# Nano-scale electronic structure of strongly correlated electron systems

Tromp, W.O.

# 5 Hydrodynamic Transport Description of the Strongly Correlated Electron System $Sr_2RuO_4$

*In sufficiently strongly interacting and clean electron systems transport phenomena are determined by hydrodynamic effects in contrast to diffusion dominated transport due to disorder. Successful efforts in showing these hydrodynamic effects relied primarily on clean systems with extremely large disorder length scales[1–3]. Here we take the opposite approach by focusing our attention on a system with a short interaction length scale, i.e. a strongly interacting system, which is still clean enough to show hydrodynamic transport. Built on a previous result[2] we propose an experiment to observe nanoscale vortices in the strongly interacting superconductor $Sr_2RuO_4$, spurred on by its cleanliness of both the bulk crystal and structured mesoscopic devices. Our calculations indicate the existence of a crossover from diffusive to hydrodynamic transport in $Sr_2RuO_4$. The crossover exists over a wide range of disorder levels, and is robust against boundary effects. These results suggest a new probe into the strongly interacting normal stat of $Sr_2RuO_4$. Implementing the calculations for a cuprate strange metal system, proposed to be hydrodynamic through holography[4], shows no hydrodynamic effects for realistic disorder levels, pointing towards the importance of disorder in strange metal systems.*

# 5.1 Introduction

The emergence of complex electronic behavior is tied to the number of electrons and the strength of their mutual interactions[5]. It is therefore reasonable to expect that transport in mesoscopic devices is a prime candidate to observe such complex behavior due to large number of electrons in such a device while still being on the small length scales at which complexity often arises (see for example the emergence of superconducting puddles in Chapter 3). One telltale sign of complex or collective behavior in mesoscopic devices is the observation of hydrodynamic transport phenomena[1,3,6–8], as these phenomena rely on a conserved momentum of all electrons involved. Such behavior however is quickly drowned out by interactions which destroy this collective momentum, such as phonon interactions or impurity scattering, reducing transport physics to single particle physics.



Transport phenomena are thus split into several regimes, based on which of the above interactions are dominant. When impurity scattering, phonon scattering, or some other momentum non-conserving interaction dominates, transport is said to be in the diffusive or Ohmic regime (**Fig. 5.1a**). In this case a sense of collective electron momentum is destroyed over length- or time scales smaller than the system being probed. A lack of conserved momentum is also the case for the second transport regime, the ballistic regime (**Fig. 5.1b**). In this regime there are no interactions present, in the sense that the time it takes for an electron to engage in any interaction (either momentum conserving or non-conserving) is larger than the time it takes for an electron to cross the system. As such, while there are no interactions to destroy the conserved momentum, there are also no interactions to establish a collective momentum. This only happens in the last regime, the hydrodynamic regime (**Fig. 5.1c**). Here electron-electron interactions dominate, conserving the total momentum of the electron fluid, while momentum non-conserving processes are largely absent within the system. The fact that the total momentum is conserved allows for more complex transport behavior to exist, with phenomena often associated with everyday fluid dynamics such as laminar flow, vortex formation, and possibly even the onset of turbulence.

Examining which transport regime is relevant is most conveniently done by estimating the relevant length scales involved. These fall into three categories. First there is the size of the system or device, typically denoted $L$. Second, there

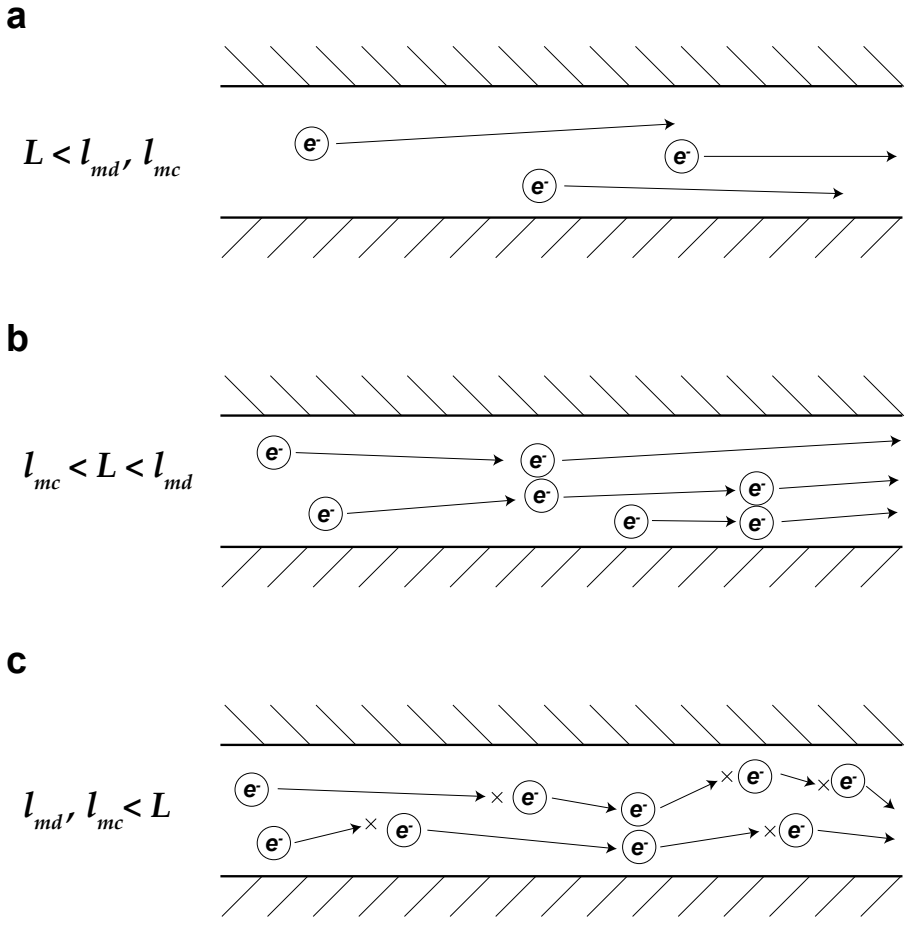


***Figure 5.1: Transport regimes.***
*Schematics of the transport regime which are determined by the relative sizes of the length scales involved.* ***a)*** *When the system size L is the smallest length scale, transport is ballistic: electrons can cross the system without scattering.* ***b)*** *When the length scale for momentum conserving scattering $l_{mc}$ is smallest, and the length scale for momentum diffusion $l_{mc}$ is largest the electron fluid as a whole carries a single conserved momentum and transport is governed by hydrodynamics.* ***c)*** *When $l_{md}$ becomes smaller than L the momentum of the electron fluid can diffuse away during transport, losing its conserved nature. Transport is now diffusive.*

is the length scale over which momentum of the electron fluid is lost to the lattice (or some other subsystem). This momentum diffusion length $l_{md}$ bundles scattering events such as impurity scattering and electron-phonon scattering (although there are exceptions to the latter[3,8]). Lastly, the momentum conserving length $l_{mc}$ characterizes the processes conserving the electron momentum fluid, typically electron-electron interactions. The system size $L$ is under control of the experimentalists, while $l_{md}$ and $l_{mc}$ depend on the materials involved and external factors such as temperature and applied pressure.

Observing hydrodynamic electron flow is no easy feat, primarily because the required combination of length scale is difficult to achieve. For hydrodynamic flow to occur $l_{mc}$ needs to be the smallest length scale, while $L$ needs to be at least on the order of $l_{md}$, if not smaller:



$$l_{mc} < L < l_{md} \tag{5.1}$$

This way the electron fluid momentum can equilibrate within the device and without being disrupted by momentum diffusion.

First attempts and successes of observing hydrodynamic flow were achieved using semiconducting systems, such as GaAs and graphene[1,2,9]. The main advantage of these systems is that $l_{md}$ can be made quite large (several microns). This way, $l_{mc} < l_{md}$ is easier to guarantee even with very little electron-electron interactions, as is the case for these semiconducting systems. Furthermore, with modern lithography tools it is possible to make devices of the right shape and dimensions out of these materials to show signatures of hydrodynamic flow. Indeed, in such devices scientists have observed a unique temperature dependence of the resistivity called the Gurzhi effect[10], the formation of backflow vortices[2,11,12], Poiseuille flow[8,13,14], and distinct effects of the device geometry on transport[15–17].

More recently, the hunt for hydrodynamic electron behavior has shifted to more complex (semi-)metallic systems, such as $PdCoO_2$, $WP_2$, and $WTe_2$[3,6,8]. Their mean free paths, while still remarkably long, are significantly shorter than those of the semiconducting systems mentioned above. Instead, their stronger electron-electron interactions, and therefore shorter $l_{mc}$, enable hydrodynamic flow. In the case of $PdCoO_2$, being an oxide system, an additional challenge is to structure the devices while preserving their $l_{md}$. Nevertheless, observations of hydrodynamic flow have offered interesting windows into these systems, in particular the observation of phonon drag in $WTe_2$[8].

The endpoint for the move towards increasingly strongly correlated systems is transport in strange metal systems. In these systems it is widely believed that the quasi-particles that would otherwise constitute electrical flow are no longer present due to the exceedingly large electron-electron interactions[18–20]. As such, any definitive theory on the nature of these systems, and transport therein, is still lacking. One proposal inspired by string theory called AdS/CFT posits on general grounds that transport is of hydrodynamic nature with an extremely low viscosity[4,21]. Observing such flow would present a major step forwards in understanding strange metal systems.

In this chapter we present a stepping stone towards hydrodynamic experiments in strange metal systems by proposing and examining experiments in the normal state Fermi liquid of $Sr_2RuO_4$. We believe that hydrodynamic flow is observable in this state due to a unique combination of lengthscales. Firstly, the normal state, albeit a Fermi liquid, is a strongly correlated one. This is evidenced by transport properties such as the strongly enhanced effective mass[22–24] or the recently observed nematic behavior[25]. Secondly, the mean free path $l_{md}$ can reach up to 1μm, remarkably long for an oxide superconductor. We will examine several device designs which can give clear evidence of hydrodynamic flow, and we will calculate the expected signatures in experiments. Finally, we will take a closer look at what such an experiment would look like for a strange metal system.



## 5.2 $Sr_2RuO_4$ as a Hydrodynamic System: the Relevant Length Scales

$Sr_2RuO_4$ is perhaps best known for its highly unconventional superconducting state emerging below a $T_c$ of 1.5K. While we focus mainly on the normal state rather than the superconducting state (reviews into the superconductivity of $Sr_2RuO_4$ can be found here[26–28]), one aspect is worth pointing out. The superconducting state is highly sensitive to disorder due to its unusual pairing symmetry (the exact pairing symmetry is still an ongoing debate[28]). This mainly shows as a reduction of $T_c$ for more disordered crystals. In fact, there is a clear relation between $T_c$ and the residual resistivity $\varrho_0$, which serves as a proxy for the amount of disorder. The $T_c$ is thus a useful diagnostic tool to determine sample quality. Samples with a $T_c$ around 1.5K have a mean

free path (extracted from $\varrho_0$) of around 1μm. It is this extremely long mean free path which motivates the choice of $Sr_2RuO_4$ as a candidate for showing hydrodynamic transport behavior.

The first of the relevant length scales, or time scales which appear more naturally in the Navier-Stokes equations, are most easily calculated from the resistivity $\varrho(T)$. As $Sr_2RuO_4$ is a quasi-2D system, with resistivity anisotropies ranging from $10^2$ to $10^3$ [24,26,29], we can use the following relation between the residual resistivity and a scattering time from Boltzmann transport[29]:

$$\rho(T) = \frac{2\pi\hbar\delta}{e^2}\frac{1}{\sum_i k_{F,i} v_{F,i} \tau_i(T)} \tag{5.2}$$



Where δ is the distance between the RuO planes and $e$ is the electron charge. $Sr_2RuO_4$ is a multiband system, with three bands called the α,β, and γ bands, so the summation runs over the Fermi vector $k_F$ and Fermi velocity $v_F$ of each of the bands, and in principle we also need to take into account that the scattering time can differ between the bands. For the latter, we will assume that the scattering time is independent of the band index, and treat this as an effective scattering time for the whole system:

$$\tau(T) = \frac{2\pi\hbar\delta}{e^2}\frac{1}{\rho(T)\sum_i k_{F,i} v_{F,i}} \tag{5.3}$$

The Fermi vectors and velocities are readily available from literature[22,23,30], as is the interplanar distance[31]. It turns out that the Fermi velocities of the three bands are roughly similar, so we can calculate a length from the scattering time by simply using an average Fermi velocity:

$$l(T) = v_F \tau(T) \tag{5.4}$$

To get a sense of the size of the device needed to observe hydrodynamic transport, we look at two different scattering processes: impurity scattering and electron-electron scattering. These two are the only relevant ones, as the low temperature resistivity behavior is purely quadratic in $T$ [29]:

$$\rho(T) = \rho_0 + AT^2 \tag{5.5}$$

At low enough temperatures impurity scattering dominates the resistivity, as this is the only process which is temperature independent. As such, the

impurity length scale $l_{md}$ is calculated using the residual resistivity $\varrho_0$ by extrapolating the resistivity to $T = 0$K. High quality $Sr_2RuO_4$ crystals can have a $\varrho_0$ as low as 0.1μΩ cm [24,32], which using the formulas above yield a length scale of $l_{md} = 960$nm.

The electron-electron scattering length $l_{mc}$ is extracted from the $T^2$ term of the total resistivity by simply plugging in $AT^2$ into equation 5.3. Using a value for $A$ of 7.3 nΩ cm/K$^2$ [33] we find an electron-electron scattering length of $l_{mc} = 60$ nm at a temperature of 15K (see **Fig. 5.2a**). Note that this length scale has a $T^{-2}$ temperature dependence, meaning this length diverges towards $T$=0. In order to observe hydrodynamic effects not only is it needed that $L < l_{md}$, but also $l_{mc} < L$. The former will be the main reason behind the size of the geometry, while the latter will determine the temperature window of the experiment. For a size of a few hundred nm, a temperature of around 15K will satisfy both conditions.



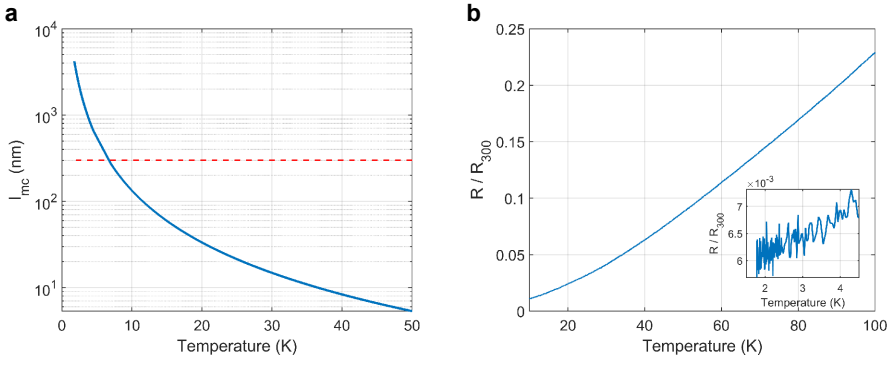


***Figure 5.2 Electron-electron length scale.***
***a)*** *The temperature dependence of the electron-electron scattering length scale associated with momentum conservation, calculated using the $T^2$ coefficient and Fermi momenta and velocities given in the main text. The red dashed lines indicates the device width of 300nm. When $l_{mc}$ exceeds the device width, which occurs at 6.7K here, transport crosses over to the ballistic regime.* ***b)*** *The resistance data used for a FIB-structured $Sr_2RuO_4$ device used in this chapter to estimate the total scattering time τ. The resistance in normalized to the room temperature value $R_{300}$. Source: Remko Fermin, private communication.*

# 5.3 Hydrodynamic Transport Simulations

*5.3.1 Momentum Diffusion in the Navier-Stokes Equation*

A more precise value for both these quantities, the geometry size and the appropriate temperature window, can be given first by examining the Navier-Stokes equations appropriate for electron flow, and solving the numerically for the envisioned device geometry. As we will see, the earlier estimates turn out to be fairly accurate.



In general, the transport behavior will be some combination of hydrodynamic effects and regular Ohmic flow. As such, the Navier-Stokes equations dealing with hydrodynamic flow are modified in the following way[2,12,17]:

$$\frac{\tau}{ne}(\mathbf{J}\cdot\nabla)\mathbf{J}+\frac{ne^2\tau}{m^*}\nabla\Phi-\nu\tau\nabla^2\mathbf{J}+\mathbf{J}=0 \tag{5.6}$$

Where $n$ is the carrier density, $e$ the electron charge, $m^*$ the effective mass, $\nu$ the kinematic viscosity, and $\tau$ the total scattering time. The variables to solve the equations for are the current density $\boldsymbol{J}(x,y)$ and the electrical potential $\Phi(x,y)$, where we use the quasi-2D nature of $Sr_2RuO_4$ to approximate as being fully 2D. The addition of the final term encodes the Ohmic behavior in our system. Furthermore, we are looking for steady-state solutions which reduces the continuity equation to:

$$\nabla\cdot\mathbf{J}=0 \tag{5.7}$$

The carrier density is calculated by using 4 electrons per unit cell[22,34] and the volume of said unit cell[31], yielding a density of $n = 2.1*10^{28}\,m^{-3}$. For the effective mass $m^*$ we will use an average of the effective mass of each band of 8.5 $m_e$. The viscosity $\nu$ is related to the length scale $l_{mc}$ through[2,12,17]:

$$\nu=\frac{1}{4}v_F l_{mc} \tag{5.8}$$

Where we again use the averaged Fermi velocity $v_F$. At a temperature of 15K, $\nu$ is roughly $0.005 m^2 s^{-1}$. This quantity, together with the total scattering time,

is temperature dependent, and the relative sizes of the two will determine the type of electron flow in the device. The scattering time $\tau$ we will estimate from the total resistivity at the temperature of interest. For this we will use the resistance data below (see **Fig. 5.2b**). Note that we will use the full resistivity. The scattering time in equation 5.6 is introduced through the inclusion of resistivity via the Ohmic term. As such, this scattering time includes any process which contributes to the resistivity. Also it is interesting to note that for the resistivity the exponent of the temperature dependence goes down at higher temperatures[29,34]. This is unusual as in regular metals electron-phonon coupling sets in at higher temperatures which as a $T^5$ dependence (below the Debye temperature which is above 400K for $Sr_2RuO_4$ [35]). The drop of the exponent is associated with the presence of a Van Hove singularity close to $E_F$ in the $\gamma$ band, which enhances scattering rates[36]. How this enhancement fits into the momentum conserving versus momentum diffusing framework is unclear. Therefore we opt to overestimate the amount of momentum diffusion and use the total resistivity for the scattering time.



The data we use to calculate the total scattering time $\tau$ is resistance data, not resistivity data. We convert between the two by assuming a value for the residual resistivity $\varrho_0$ and scale the finite resistivity according to the resistance data. This also means that $\varrho_0$ is a free parameter of the simulations. We will use this to get a sense of the influence of disorder on the backflow.

Equation 5.6 features a new length scale as the coefficient of the Laplacian term:

$$D_\nu = \sqrt{\nu\tau} = \frac{1}{2}\sqrt{l_{mc} l_m d} \tag{5.9}$$

This length scale determines the size of the hydrodynamic effects. The size of the geometry needs to be large enough to accommodate this, while the size of the probes (the contacts used to measure the hydrodynamic effects) needs to be small enough to be sensitive to this size. For the estimates given in section 5.2 $D_\nu$ is 120nm. This is thankfully compatible with the earlier estimate for the geometry size.

For the device geometry we propose to use the vicinity geometry, which was originally proposed and used to demonstrate the presence of hydrodynamic effects in graphene[2]. In this setup the current is injected into the device through a small opening (see **Fig. 5.3a**). When the flow follows solely Ohm's law the current follows the edges of the device (**Fig. 5.3b**). When hydrodynamic effects

are present, a negative pressure directly next to the point of injection causes the formation of a backflow or whirlpool (**Fig. 5.3c**). As such, the current flows in a different direction depending on the transport regime, and the voltage across two contacts where the backflow can occur will have the opposite sign. The change of sign is the signature of crossing over from purely Ohmic behavior to hydrodynamic behavior.

Important in considering which geometry to use is considering what type of hydrodynamic flow is expected, codified in the Reynolds number:

$$RE = \frac{uL}{\nu} \tag{5.10}$$



For low Reynolds numbers (<1) the flow will be laminar, while for high Reynolds number (>1000) the flow will be dominated by turbulent effects, with a crossover or pre-turbulent regime for intermediate values. The fluid velocity is given by the drift velocity $u = J/ne$, on the order of $10ms^{-1}$ for a total current of 1mA in mesoscopic devices. The typical length scale is order 100nm, and using a viscosity of $\nu = 0.005m^2s^{-1}$ gives a Reynolds number of $RE = 2*10^{-4}$. This means the flow will be deep in the laminar regime. As such, many effects associated with hydrodynamics will not occur in $Sr_2RuO_4$. In particular, experiments relying on the merging several flow paths will not show the desired effects, as we demonstrate in Appendix 5A.

The geometry we use in our simulation has a main channel with a length $L$ and a width $H$ of 1μm and 300nm respectively. The current injector has a width $W$ of 50nm, same for the voltage contacts used to measure the backflow voltage. Devices of $Sr_2RuO_4$ of such sizes can be fabricated using state-of-the-art techniques, by first exfoliating a bulk crystal into film flakes and then by creating the structure with focused ion beam milling (FIB), which has been shown to preserve the sample quality as measured by ratio of low temperature and high temperature resistance[37]. Using thin flakes for the device, a necessity for using FIB, has the added benefit of increasing the current densities, which enhances the voltage signal. We will assume a flake thickness of 500nm for the conversion between current density and total current.

*5.3.2 COMSOL Implementation*

We numerically solve equation 5.6 for this geometry using the COMSOL Coefficient Form PDE interface. This package solves a general PDE of the

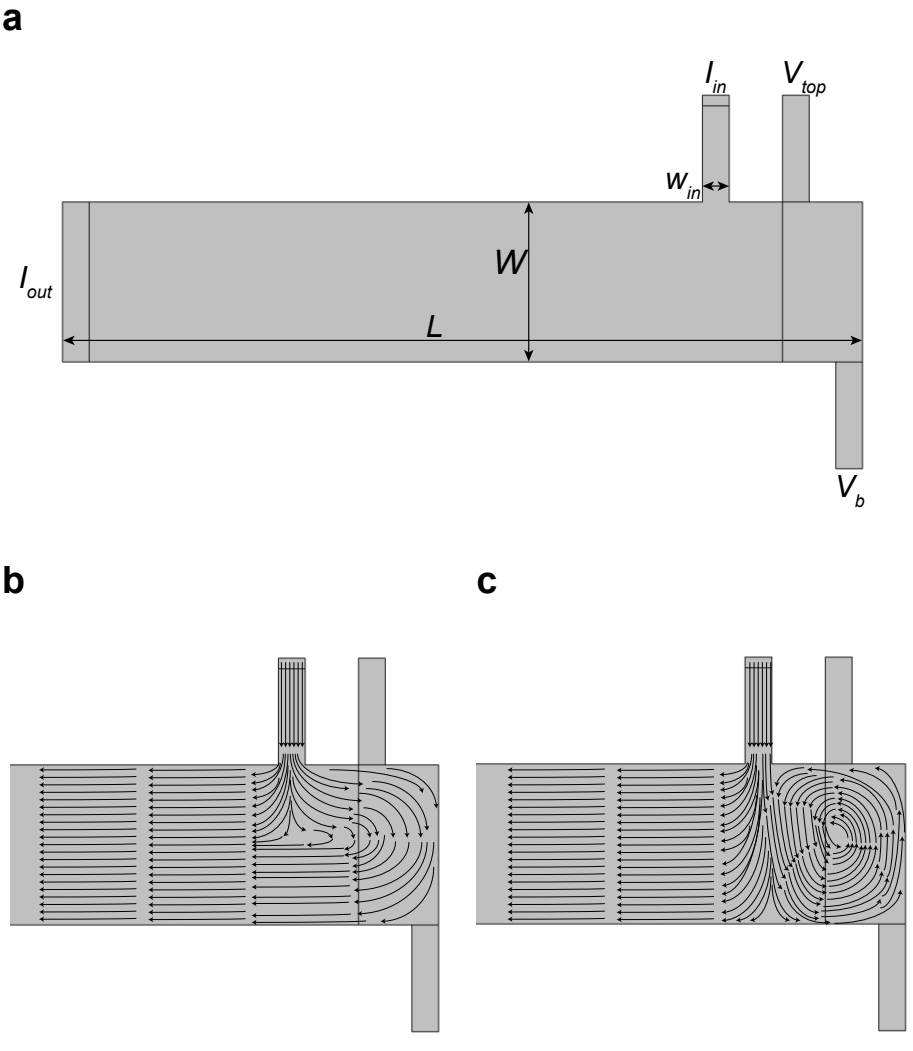


***Figure 5.3 The vicinity geometry.***
***a)*** *The geometry of the device as used in the COMSOL simulations. The current enters the main device of width W and length L through the contact $I_{in}$ of width $w_{in}$ and flows out of the device at $I_{out}$. The backflow voltage is measured between the contacts $V_{top}$ and $V_{bot}$. The sign of this voltage depends of the flow regime. In the diffusive or Ohmic regime shown schematically* ***b)*** *this voltage is positive as the current flows from $V_{top}$ to $V_{bot}$. In the hydrodynamic regime depicted in* ***c)*** *the sign reverses as the backflow reverses direction due to the formation of negative pressure immediately next to $I_{in}$.*

following form for a user defined geometry:

$$e_a \frac{\partial^2 u}{\partial t} + d_a \frac{\partial u}{\partial t} + \nabla \cdot (-c\nabla u - \alpha u + \gamma) + \beta \cdot \nabla u + au = f \qquad (5.11)$$

Where *u = (u1,u2,u3)* is the vector containing the independent variables, ($\sigma\Phi$,$J_x$, $J_y$) in our case. This equation maps onto equations 5.6 and 5.7 by setting the coefficients as follows:

$$\begin{gathered} e_a = d_a = \alpha = \gamma = f = 0 \\ a = \begin{pmatrix} 0 & 0 & 0 \\ 0 & 1 & 0 \\ 0 & 0 & 1 \end{pmatrix} \\ c = \begin{pmatrix} 0 & 0 & 0 \\ 0 & \nu\tau & 0 \\ 0 & 0 & \nu\tau \end{pmatrix} \\ \beta = \begin{pmatrix} \begin{pmatrix} 0 \\ 0 \end{pmatrix} & \begin{pmatrix} 1 \\ 0 \end{pmatrix} & \begin{pmatrix} 0 \\ 1 \end{pmatrix} \\ \begin{pmatrix} 1 \\ 0 \end{pmatrix} & \frac{\tau}{ne}\begin{pmatrix} u_2 \\ u_3 \end{pmatrix} & \begin{pmatrix} 0 \\ 0 \end{pmatrix} \\ \begin{pmatrix} 0 \\ 1 \end{pmatrix} & \begin{pmatrix} 0 \\ 0 \end{pmatrix} & \frac{\tau}{ne}\begin{pmatrix} u_2 \\ u_3 \end{pmatrix} \end{pmatrix} \end{gathered} \qquad (5.12)$$

The boundary conditions are set so that no current flows through the edges of the sample, and that the flow along the edges is allowed to slip, encoded via a slip-length:

$$\begin{gathered} \mathbf{J}_\perp = 0 \\ \mathbf{J}_\parallel = L_{slip} n \cdot \nabla \mathbf{J}_\parallel \end{gathered} \qquad (5.13)$$

Where is the current perpendicular to the boundary, the current along the boundary, and $n$ the vector normal to the boundary. The slip-length $L_{slip}$ captures the interaction between the boundary and the fluid. Using a slip-length allows us to interpolate between two commonly used boundary conditions in fluid mechanics: no-slip condition ($L_{slip}$ = 0) and no-stress condition ($L_{slip}$ to infinity). This does come at the cost of another parameter

whose value is initially unknown. An estimate for $L_{slip}$ can be given through the following argument[38]: The slip-length should encode interactions with the boundary. Therefore for distances to the boundary smaller than the slip-length electrons are more likely to scatter off the boundary than off anything else (including other electrons). The estimate for the slip-length is then the smallest of the scattering length scales of the system, in our case the electron-electron scattering length. In our simulations we will use a temperature independent slip-length of $L_{slip}$ = 50nm. At the current inlet and outlet we fix the potential, being 1mV at the inlet and 0mV at the outlet. Fixing the potential drop over the device turns out to give the least artifacts at the current inlet and outlet, though in principle it is also possible to fix the total current through the device and measure the potential drop between inlet and outlet.

The temperature dependence of the backflow voltage is solely determined by the temperature dependence of the viscosity $\nu$ and the scattering time $\tau$. The temperature dependence of the former is $T^{-2}$ via equations 5.4 & 5.8, and the temperature dependence of the latter is given by the resistance data used to extract the scattering time. For each temperature point we calculate these two quantities and use them to simulate the flow profile of the vicinity geometry. From this we calculate the backflow voltage between the two voltage contacts. Finally we express the result as a backflow resistance by dividing the backflow voltage by the total current injected. The reason to do this is that by fixing the voltage drop between the current contacts via the boundary conditions the total current can in principle vary as a function of temperature. This effect is separated out by using the backflow resistance as the final result. Then we repeat the simulations for various values of $\varrho_0$ to examine the effects of disorder on the result.



# 5.4 Hydrodynamic Transport in $Sr_2RuO_4$

### *5.4.1 Negative Backflow Resistance*

The results of the $Sr_2RuO_4$ simulations are shown in **Fig. 5.4** and **Fig. 5.5**. In **Fig. 5.4a** we show current distributions typical for the high temperature (**Fig. 5.4a**) and the low temperature (**Fig 5.4b**) transport behaviour in the backflow section of the device. The distributions are qualitatively different, having

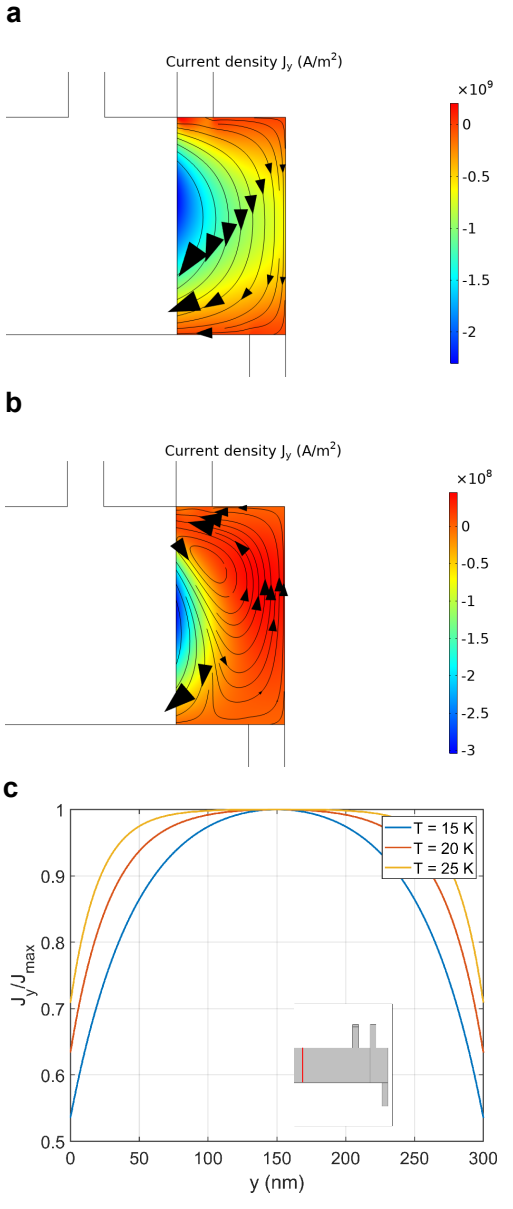


***Figure 5.4 $Sr_2RuO_4$ Flow Profiles .***
***a,b)*** *The flow profiles in the backflow section of the device at high temperature (T=25K) and low temperature (T=5K) resp. for $\rho_0 = 0.25\mu\Omega cm$. The appearance of a whirlpool at low temperature marks a qualitative difference between the two transport behaviors.* ***c)*** *The flow profiles for $J_y$ across the main channel of the device as a function of temperature for the same $\rho_0$. At low temperature the flow follows a roughly parabolic profile which flattens out as the temperature increases. The red line in the inset shows the line on the geometry along which $J_y$ is measured.*

an opposite flow direction in the two different regimes. The emergence of a whirlpool at low temperature is a sign of hydrodynamic dominated transport. The crossover between these two regimes is also apparent from the current distribution across the main channel of the device in **Fig 5.4c**. The high temperature calculation shows a nearly flat distribution, dropping near the edges of the device. As the temperature is lowered the distribution smoothly deforms towards the parabolic Poiseuille flow typical for hydrodynamic transport. The finite current at the boundaries is a result of the finite $L_{slip}$ used in the simulations. The smooth evolution of the current distributions emphasizes that in general the transport is a mixture of both Ohmic and hydrodynamic effects, and any calculation needs to address them simultaneously.

The crossover from Ohmic to hydrodynamic transport, and the influence of disorder on the crossover, is apparent in both the forward and backflow resistances of the device shown in **Fig. 5.5**. In **Fig. 5.5a** we show the total or forward resistance of the device, calculated by measuring the total injected current and dividing by the 1mV potential drop fixed as boundary conditions. At low temperatures the resistance shows an upturn with decreasing temperature, departing from more usual metallic behavior at higher temperatures. This upturn is reminiscent of the Gurzhi effect[10], one of the signs of hydrodynamic behavior.



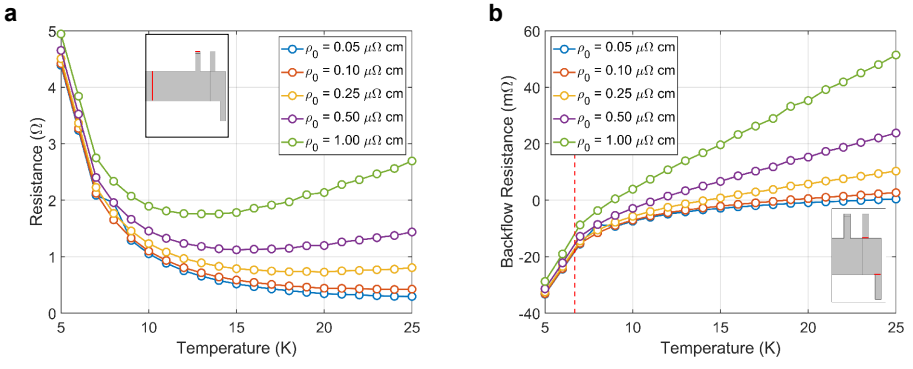


***Figure 5.5 $Sr_2RuO_4$ Backflow resistance.***
***a)*** *The total resistance of the device as a function of temperature for multiple values of $\rho_0$, using the current flowing through the red lines shown in the inset. The upturn in the resistance is a sign of hydrodynamic effects[10].* ***b)*** *The backflow resistance for the $Sr_2RuO_4$ vicinity geometry for various values of the residual resistance $\rho_0$. A positive resistance is indicative of the diffusive regime, a negative resistance of hydrodynamic regime (see* ***Fig. 5.3****). The red line indicates the temperature below which ballistic effects set in[2,39] (see* ***Fig. 5.2a****). The inset shows the vicinity geometry, with the red lines showing where the voltage is measured.*

The crossover is perhaps most evident when looking at the backflow resistance shown in **Fig. 5.5b**. At higher temperature we find a positive backflow resistance, consistent with Ohmic transport. As the temperature drops, the backflow resistance eventually drops below zero, indicating a crossover into the hydrodynamic regime. The temperature at which the zero crossing occurs depends on the level of disorder in the device, encoded in $\varrho_0$. For clean samples ($\varrho_0$ = 0.1 μΩ cm) the crossover occurs at T=19K, a temperature which drops to T=9K for $\varrho_0$ = 1μΩ cm. This is a surprisingly broad range of disorder levels at which the crossover should still be observable. While this wide margin seems to offer some leniency for the fabrication processes of the samples, some care should be taken with this result. At the top of this range ($\varrho_0$ = 1μΩ cm) the $T_c$ of bulk $Sr_2RuO_4$ has dropped to zero due to disorder[26]. This dramatic change due to disorder warrants a more careful look into the appropriate transport description when $l_{mc}$ roughly equals $l_{md}$.



When the temperature drops even further, the geometry size becomes the smallest length scale of the system. The flow becomes predominantly ballistic characterized by an upturn in the backflow resistance as the temperature is reduced[2,39]. While the backflow resistance remains negative during this upturn, the system is in a quasi-ballistic regime where interaction still play a role[39]. Fully ballistic transport sets in when the backflow resistance becomes positive. The physics of the crossover between hydrodynamic and ballistic, governed by the Knudsen number $Kn = l_{mc}/L$, is not captured in our transport description., though we can estimate when it occurs: $l_{mc} = L$ occurs at roughly 6.5K, marked by the red dashed line in **Fig. 5.5b**.

*5.4.2 Boundary Effects: the Slip-length*

There is still one free parameter left unexamined: the slip-length $L_{slip}$. To study its effect on the backflow voltage we fix the total scattering time to $\tau = 1*10^{-10}$ s and the temperature to T=15K so that we are in the hydrodynamic regime where we expect $L_{slip}$ to have the largest effect. We then vary $L_{slip}$ over a range of 1nm to 1μm. **Fig. 5.6a,b** show the backflow patterns for both $L_{slip}$ = 1nm and $L_{slip}$ = 1μm. We find that while the exact size and shape of the whirlpool does change with the slip length, its presence is remarkably stable against a changing $L_{slip}$. Over a range of at least 3 orders of magnitude we still expect a negative backflow resistance. To check that the slip length is indeed properly incorporated we show the flow distributions across the main channel in **Fig. 5.6c** and find that indeed the curvature of the distribution flattens and the

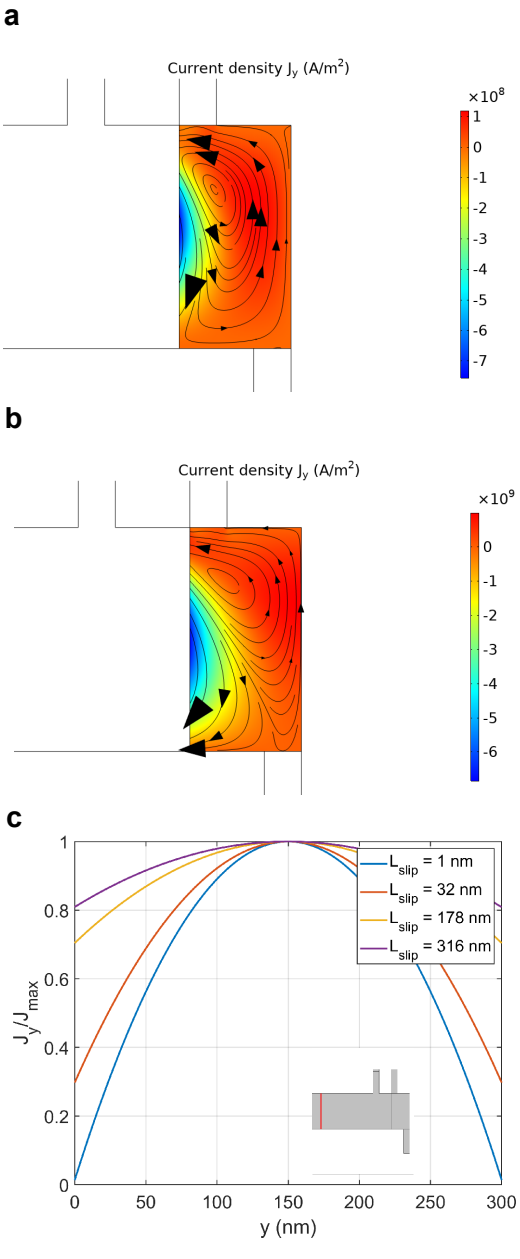


***Figure 5.6 $L_{slip}$ dependent Flow Profiles.***
***a,b)*** *The flow patterns in the backflow section of the device for $L_{slip}$ = 1nm and $L_{slip}$ = 1µm respectively. Despite the large difference in $L_{slip}$ the flow direction remains stable.* ***c)*** *The flow profile across the main channel of the device for several values of $L_{slip}$. The flattening of the profile and the increasingly large current along the boundaries are consistent with a gradual change from no-slip conditions to no-stress conditions.*

current at the boundary increases for larger $L_{slip}$, consistent with a change from no-slip boundary conditions ($L_{slip} = 0$) towards no-stress boundary conditions ($L_{slip}$ towards infinity). The changes in the current distribution due to the slip length imply that the forward resistance does not have a similar stability as the backflow resistance seems to have.

These two predictions about the forward and backflow resistances are confirmed in **Fig. 5.7** where we show the effect of $L_{slip}$ on the forward and backflow resistance. The total resistance shows a strong dependence of the slip length, as we expected from **Fig. 5.6c**. The drop in resistance as $L_{slip}$ increases can be attributed to the decreased curvature of the flow profile, as the friction between adjacent fluid layers decreases when their relative velocity decreases. As anticipated from **Fig. 5.6a,b** the backflow resistance indeed remains negative over the full range of slip lengths. Not only that, its magnitude also remains nearly unchanged. The remarkable stability of the backflow resistance against the slip length improves the feasibility of a vicinity geometry experiment. Determining the slip length experimentally is quite difficult, especially when the flow profile cannot be directly measured. The fact that $L_{slip}$ does not influence not only the sign but also the magnitude of the backflow resistance eliminates the need for an accurate determination of $L_{slip}$.

These result together indicate that hydrodynamic effects on the low temperature transport of $Sr_2RuO_4$ are not only possible in principle, but also fall within the technical abilities of modern experimental techniques. The approach we use

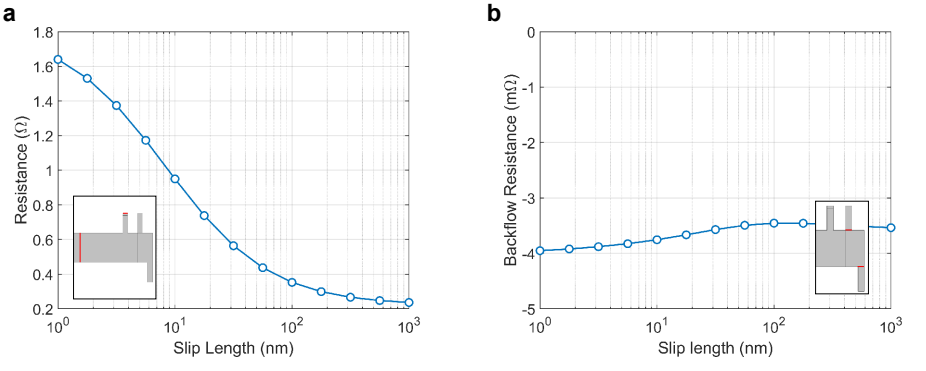


***Figure 5.7 $L_{slip}$ dependent resistances.***
***a)*** *The total resistance of the device as a function of slip length. The resistance shows a strong dependence resulting from the changing current distribution as the slip length changes.* ***b)*** *The backflow resistance as a function of slip length. Remarkably, the backflow resistance remains nearly constant over a wide range of values for $L_{slip}$, despite the changes in the total resistance.*

to calculate the backflow resistance also offer a degree of internal consistency with future experiments, as most important input parameters (such as the residual resistivity $\varrho_0$ and the $T^2$ coefficient) can be extracted from a simple R-T curve of the crystal the device is created from. The use of COMSOL allows for more realistic simulations as the exact device geometry is more easily incorporated in the simulations. Since the existence of hydrodynamic effects rely heavily on the presence and the strength of electron correlations the observation of the effects described above offer a novel window into the correlated physics of $Sr_2RuO_4$. It would also represent a step forwards for the use of hydrodynamics in the description and probing of correlated electron systems, for which other transport frameworks may fall short.

## 5.5 Towards Strange Metal Hydrodynamics



### *5.5.1 Transport Parameters*

One example of such a system, and an extreme example of a correlated system, is a strange metal. This metallic phase, characterized by a linear-in-T resistivity for all temperatures, is most well known as the normal state of cuprate superconductors at optimal doping[19,40], although it is also found in other strongly correlated superconductors[41–43]. One important aspect of the linear-in-T resistivity is that it violated the Mott-Ioffe-Regel limit, defined as the resistivity at which the mean free path is on the same order as the lattice constant[44]. This violation seems to imply that the current is not carried by the quasi-particles we have come to expect from a Fermi liquid. This striking hypothesis is supported by ARPES experiments which find a clear lack of quasi-particles[18,20]. How to deal with this absence of quasi-particles and how to describe the (transport) properties of such a system is one of the most profound mysteries of correlated electron physics.

One proposal makes use of the AdS/CFT correspondence[4,21]. This mathematical machinery creates a bridge between certain models in general relativity (Anti-de Sitter spaces, the AdS part) and certain quantum theories (conformal field theories, the CFT part). The idea being that a hard problem on one side of the bridge translates to a more tractable problem on the other side. Then after solving the more tractable problem, the solution is translated

back. In particular, one can create metallic systems with this construction with properties reminiscent of strange metal behavior, particularly the linear-in-T resistivity. Additionally, transport in these systems is governed by the laws of hydrodynamics. In what follows we sketch what an experiment using the vicinity geometry would look like for a strange metal system with properties deriving from the AdS/CFT correspondence. We will follow the review ref[4] when determining the relevant hydrodynamic system parameters.

A core concept of the AdS/CFT strange metal is minimal viscosity. Metals in this phase have a very particular relation between their dynamic viscosity $\eta$ and their entropy density $s$:

$$\frac{\eta}{s} = A\frac{\hbar}{k_b T} \tag{5.14}$$



Where A is some numerical prefactor, equal to $1/4\pi$ in the AdS/CFT setting, although real system have a value closer to 1. The entropy density takes a Sommerfeld like form of

$$s = \frac{k_b^2 nT}{\mu} \tag{5.15}$$

with $n$ the number density, and $\mu$ the chemical potential. This leads to the following expression for the kinematic viscosity $\nu$ which we will use in our simulations:

$$\nu = \frac{A\hbar k_b T}{m_e \mu} \tag{5.16}$$

Where we used the mass density $\varrho = nm_e$ to convert the dynamic viscosity $\eta$ to the kinematic viscosity $\nu$. Plugging in the numbers, we find a viscosity of $\nu = 2*10^{-7} m^2 s^{-1}$, using $\mu$ = 1eV appropriate for optimally doped cuprates[45], 4 orders of magnitude lower than the $Sr_2RuO_4$ case! This also means that the Reynolds number $RE$ is 4 orders of magnitude larger, meaning it is on the order of 1. This means that pre-turbulent phenomena might be an possibility.

There is a scattering time associated with the minimal viscosity under the name of Planckian dissipation:

$$\tau = A\frac{\hbar}{k_b T} \tag{5.17}$$

However, even a strange metal system is not immune to disorder scattering. In fact, the cuprates, perhaps the most well-known example of a strange metal system, is notorious for its high levels of disorder. The highest quality cuprate samples have a residual resistance of $\varrho_0 = 1.5\mu\Omega$cm in the case of $La_{2-x}Sr_xCuO_4$ [46]. This is remarkably low for a cuprate, but still an order of magnitude worse than $Sr_2RuO_4$. Translating this to a scattering time, this corresponds to $\tau = 1.8*10^{-12}$s.

*5.5.2 Absence of Whirlpool Formation*

In our simulations for the strange metal system, we will use the same geometry size as the $Sr_2RuO_4$ case, as this size is already pushing the limitations of modern FIB techniques. Unlike the $Sr_2RuO_4$ we will assume a temperature independent scattering time given by the residual resistivity $\varrho_0$, representing a more optimistic scenario compared to including Planckian dissipation into $\tau$. Also unlike the previous simulations we no longer fix the potential drop over the device. Instead we fix the total current flowing through the device. As such we have better control over the Reynolds number during the simulations, and we can avoid accidentally entering the turbulent regime as a result of a sudden increase in the current due to a drop in the forward resistance when hydrodynamic effects take over. The drawback is that fixing the current through the device is more susceptible to artifacts in the current distribution, as can be seen in **Fig 5.8a**, where the flow through the main channel of the device is skewed to one side of the channel.

Using a value of $\nu = 1*10^{-7}m^2s^{-1}$, $\tau = 1.8*10^{-12}$s, and $L_{slip} = 50$nm, our simulation yields the flow distribution shown in **Fig. 5.8a**. This flow profile is consistent with Ohmic transport, meaning the higher levels of disorder has drowned out the effects of the minimal viscosity. To observe a sign of the minimal viscosity, we show the flow profile for $\tau = 1.8*10^{-10}$s and $\tau = 1.8*10^{-9}$s in **Fig. 5.8b,c**. In the former case the first signs of a whirlpool emerge, but it fails to encompass the entirety of the backflow section, meaning the backflow resistance is most likely still positive in this case. Only when the scattering time is increased higher does the whirlpool cover the full width of the geometry, and do we expect a negative backflow resistance. It is also only for these values of $\tau$ that we see the effects of minimal viscosity. The higher Reynolds numbers associated with this flow shows itself through the emergence of additional whirlpools on the left of the current injector. In this case it is worth considering adding additional voltage contacts on the left of the current injector to check whether these additional whirlpools indeed appear.

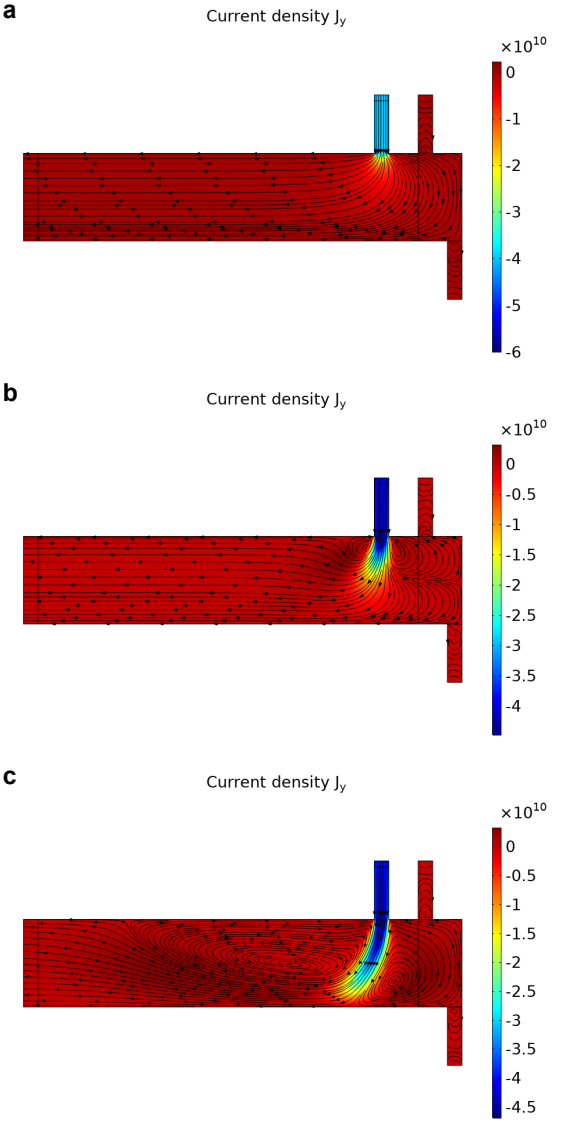


***Figure 5.8 Minimal Viscosity Flow Profiles.***
*Flow profiles in the vicinity geometry using minimal viscosity and a scattering time of* $\tau = 1.8*10^{-12}$*s,* $1.8*10^{-9}$*s, and* $1.8*10^{-8}$*s (**a,b,c** respectively). The extremely low viscosity requires large scattering times for hydrodynamic effects to appear.*

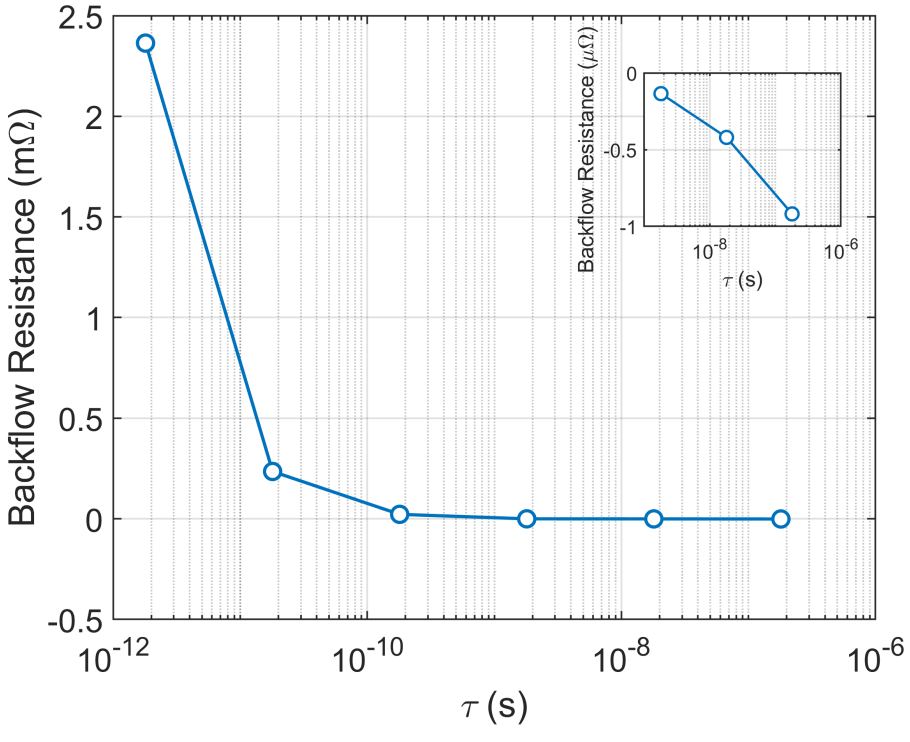


***Figure 5.9 Minimal Viscosity Backflow Resistance.***
*The backflow resistance as a function of scattering time using a viscosity $\nu = 1*10^{-7}m^2s^{-1}$ in line with minimal viscosity. The inset shows the backflow resistance for the highest values of $\tau$, where the resistance changes sign.*

The difficulty of observing hydrodynamic flow for a minimal viscosity system is summarized in **Fig 5.9**, where we show the backflow resistance as a function of scattering time for the above simulations. A negative backflow resistance would require extremely large scattering times, unrealistic not only for cuprate systems but for any system. These difficulties can be traced back to the length scale $D_\nu$ over which hydrodynamic effects can be seen. For systems much larger than this, Ohmic effects dominate. For $\nu = 1*10^{-7}m^2s^{-1}$ and $\tau = 1.8*10^{-12}s$, realistic values for a cuprate system, $D_\nu = 5Å$, barely two unit cells! Only when $\tau$ increases by several orders of magnitude does this length scale approach the system size. It turns out that the extremely low viscosity might actually be a drawback in a system that also includes disorder. The linear temperature dependence of $\nu$ is too slow to make much of a difference, even when ignoring any detrimental temperature dependence of $\tau$.

These results stress the importance of disorder in strange metal systems. Taking a straight forward approach to the role of disorder, similar to the approach for Fermi liquid systems, we find that hydrodynamic effects get washed out by disorder for a strange metal system. A more detailed examination of disorder in holography or other strange metal descriptions will need to determine whether such a straight-forward approach is warranted. Despite this negative result, we still believe it is worth performing such an experiment for a strange metal system. Given how little is known for certain about these system, any new information is valuable even if it is the absence of hydrodynamic transport. We also remark that this result is a consequence of the proposed minimal viscosity. In the hypothetical case that the viscosity of a strange metal is more in line with that of a Fermi liquid (such as $Sr_2RuO_4$) hydrodynamic transport would become more likely.



# 5A Appendix

The low Reynolds number for a Fermi liquid ($RE \sim 1*10^{-4}$, see Chapter 5.3) limits the design space for experiments attempting to show hydrodynamic transport. An illustrative example is the Tesla valve[47](**Fig. 5A.1**), a one-way valve without any moving parts. The operating principle relies on splitting off the flow into a main channel and an arced section, and merging again the two parts of the flow. How much flow is split off and how the two flows merge is fully controlled by the exact design. When properly designed, the Tesla valve has an easy axis, where only a small part is split off and the flow resistance is low (**Fig. 5A.1a**), and a hard axis, where more flow is split off and the flow resistance is higher (**Fig. 5A.1b**). However as we demonstrate this design is unsuitable for the demonstration of hydrodynamic transport in Fermi liquids, as it relies on higher Reynolds numbers.

To do so we will simulate the liquid flow through a nm sized Tesla valve. We will use a viscosity typical of $\nu = 0.005 m^2 s^{-1}$ typical for $Sr_2RuO_4$ and vary the Reynolds number by varying the flow velocity. We will only simulate hydrodynamic behavior, meaning we will omit the last term of eq. 5.6 from the simulations. This allows us to use the standard COMSOL hydrodynamics package, speeding up the calculation drastically. We will pick the size of the Telsa valve such that inequality 5.1 is still satisfied, despite momentum diffusion being absent from the simulation. The width of the Tesla valve we

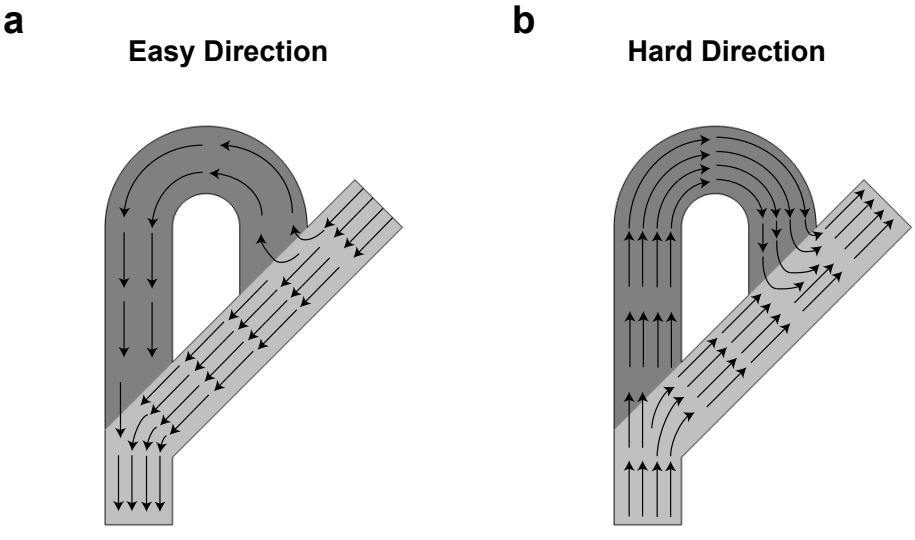


***Figure 5A.1 Tesla Valve Geometry.***
*Sketch of the Tesla valve geometry and the flow along the easy (**a**) and the hard (**b**) flow direction. The difference in split and subsequent merger of flow between the two directions result in a different resistance between the two.*

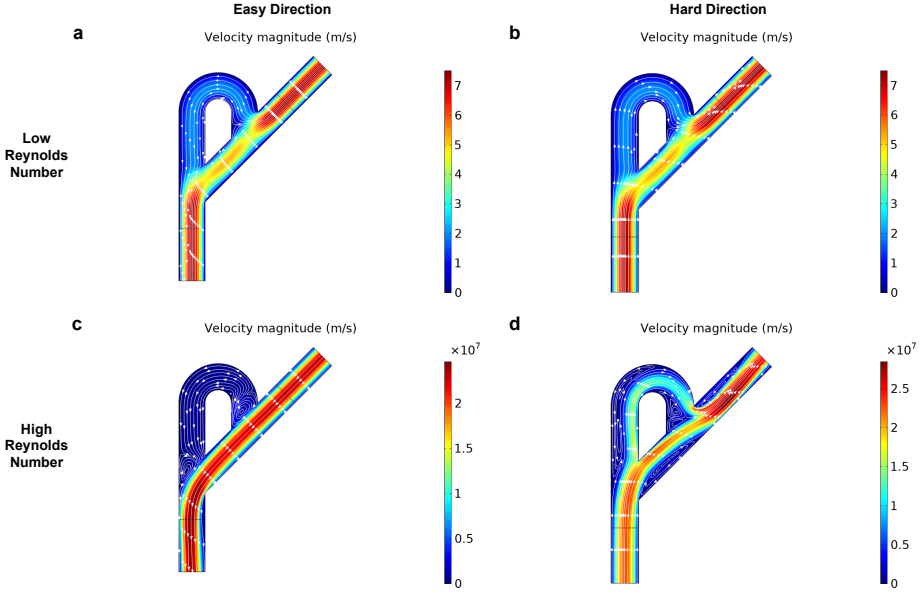


***Figure 5A.2 Tesla Valve Flow Profiles.***
*Flow profiles through the Tesla valve for the easy (**a,c**) and hard (**b,d**) directions for RE = 1*10$^{-4}$ (**a,b**) and RE = 316 (**c,d**). Only for the higher RE does the proposed diode function occur.*

set to be 100nm. The length of the loop arm is 200nm, and the loop itself has an inner radius of 50nm. The flow velocity will range from roughly $u = 10ms^{-1}$ ($RE \sim 1*10^{-4}$) to $u = 1*10^{7}ms^{-1}$ ($RE \sim 1*10^{2}$).

In **Fig. 5A.2** we show the results for these simulations for flow in the easy and hard direction for both low Reynolds number ($RE = 1*10^{-4}$, **Fig. 5A.2 a,b**) and high Reynolds number ($RE = 316$, **Fig. 5A.2 c,d**). We find that in the low *RE* case the flow profiles in the easy and hard direction look very similar, meaning that their associated flow resistances are also very similar. This implies that in this case the Tesla valve does not act as a diode as it was designed to do. The case of high *RE* is quite different. Here, the flow profiles show large differences between the two flow directions. This can be attributed to the formation of whirlpools at the points where the flow is split off and merged. The size of the whirlpools depend significantly on the overall flow direction. As such we can expect the Tesla valve to function as a diode in this regime.



We can put the expectations about diode function on more solid ground by quantifying the flow resistance for each calculated flow profile. This can be done by using[17]

$$R_\nu = \frac{\nu\rho d}{2I^2}\int \sum_{i=1}^{2}\sum_{j=1}^{2}\left(\frac{\partial v_j}{\partial x_i}+\frac{\partial v_i}{\partial x_j}\right)^2 d^2x \tag{5A.1}$$

Where $\nu$ is the kinematic viscosity, ϱ the fluid mass density, $d$ the device thickness, and $I$ the total current flowing through the device. The dependence of the exact flow profile is captured by taking the integral running over the full geometry of the derivatives of the fluid velocity $v_{x,y}$ with respect to the spatial coordinates $x,y$. We can use this expression to define a measure of how well the Tesla valve acts as a diode, the diodicity:

$$D = \frac{R_{\nu,hard}}{R_{\nu,easy}} \tag{5A.2}$$

This quantity solely depends on the shape of the fluid profiles, as all the prefactors to the integral in eq 5A.1 cancel out (the total current we keep the same when switching between easy and hard flow axis). A diodicity of $D = 1$ means there is no difference between the flow directions, and the valve does not work, while $D > 1$ means the Tesla valve works as intended. For each Reynold number we simulate we calculate the diodicity $D$, and track its evolution as a function of Reynolds number. The results are shown in **Fig.**

**5A.3**. We find that at low Reynolds numbers $D = 1$, as we anticipated from **Fig. 5A.2 a,b**. Only at roughly $RE = 20$ does the diodicity deviate from 1, reaching a value of 2.14 for $Re = 316$, the flow shown in **Fig. 5A.2 c,d**.

From this we conclude that the Tesla valve only works for moderate Reynolds number >10. The space to change the Reynolds number for a Fermi liquid system is only limited, meaning this geometry design is unsuitable for $Sr_2RuO_4$ systems. The limited space is a result of all three components of the Reynolds number being subject to limitations. The system size $L$ is limited by having to satisfy inequality 5.1, typically meaning there is at most 1 order of magnitude design space. The fluid viscosity $\nu$ is a system property whose temperature dependence is of little help as there is only a limited temperature range over which hydrodynamic flow is present. This leaves the fluid velocity $v$, given by the current through the device. A fluid velocity of roughly $10ms^{-1}$ ($RE \sim 1*10^{-4}$)



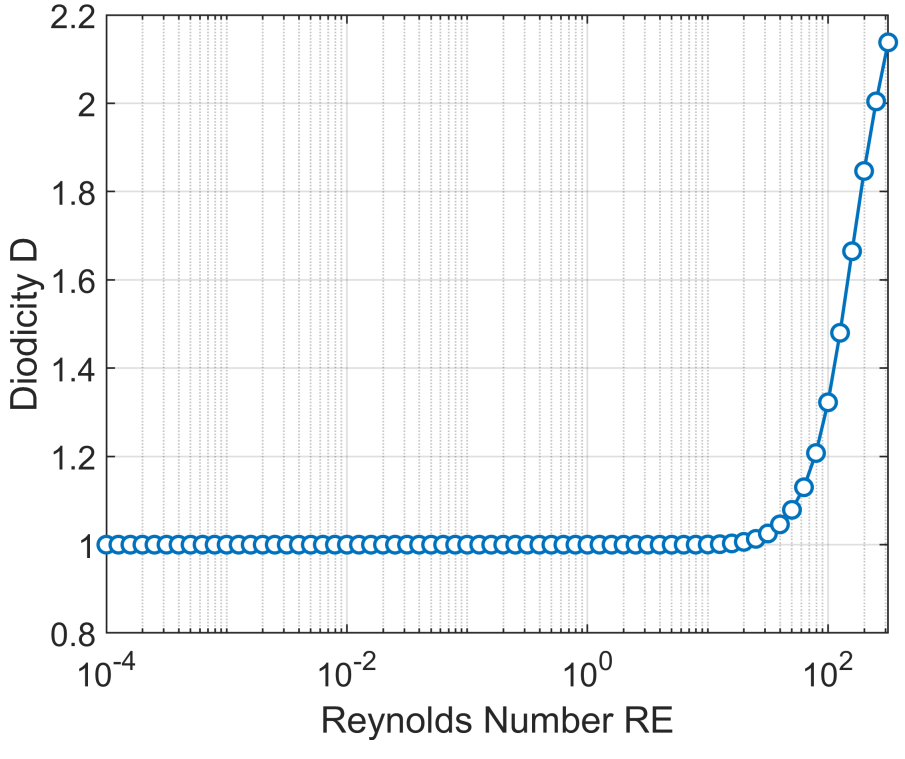


***Figure 5A.3 Diodicity.***
*Diodicity D of the Tesla valve as a function of the Reynolds number RE. The onset of diode functionality (D>1) only occurs around RE=20, much larger than the RE=$10^{-4}$ typical for flow in a Fermi liquid system.*

corresponds to a total current of roughly 1mA. This would have to increase by 4 order of magnitude to 10A to start seeing some sort of diode function, a current which a mesoscopic device will typically not survive.

This is exemplary for the limited design space for hydrodynamic experiments for Fermi liquid systems caused by an extremely low Reynolds number and little room to increase it. Hydrodynamic flow is most pronounced when whirlpools start to form, an effect unique to the hydrodynamic regime. These only start to appear generically at moderate Reynolds numbers. Deep in the laminar regime the geometry has to be design specifically to allow for a whirlpool to form. The vicinity geometry achieves this by forcing the fluid to flow through a very narrow constriction, whereas the Tesla valve solely relies on the Reynolds number for whirlpool formation.



Interestingly, the minimal viscosity proposed for strange metals opens more design space at first glance. The extremely low viscosity means that the Reynolds number is automatically higher, already having $RE \sim 1$ for $v \sim 10 ms^{-1}$, a velocity at which a Fermi liquid is still deep within the laminar flow regime. The effects of this comparatively high Reynolds number on the formation of whirlpools is clear by comparing **Fig. 5.4b** and **Fig 5.8c** This is however discounting the limits placed by the presence of momentum diffusion discussed in Chapter 5.4.

# 5.6 References

[1] de Jong, M. J. M. & Molenkamp, L. W. Hydrodynamic electron flow in high-mobility wires. *Phys. Rev. B* **51**, 389–402 (1995).

[2] Bandurin, D. A. *et al.* Negative local resistance caused by viscous electron backflow in graphene. *Science* **351**, 1055–1058 (2016).

[3] Gooth, J. *et al.* Thermal and electrical signatures of a hydrodynamic electron fluid in tungsten diphosphide. *Nat. Commun.* **9**:4093 (2018).

[4] Zaanen, J. Planckian dissipation, minimal viscosity and the transport in cuprate strange metals. *SciPost Phys.* **6**, 061 (2019).

[5] Anderson, P. W. More is Different. *Science* **177**, 393–396 (1972).

[6] Moll, P. J. W., Kushwaha, P., Nandi, N., Schmidt, B. & Mackenzie, A. P. Evidence for hydrodynamic electron flow in $PdCoO_2$. *Science* **351**, 1061–1064 (2016).

[7] Lucas, A. & Fong, K. C. Hydrodynamics of electrons in graphene. *J. Phys. Condens. Matter* **30**, 053001 (2018).

[8] Vool, U. *et al.* Imaging phonon-mediated hydrodynamic flow in $WTe_2$. *Nat. Phys.* **17**, 1216–1220 (2021).

[9] Crossno, J. *et al.* Observation of the Dirac fluid and the breakdown of the Wiedemann-Franz law in graphene. *Science* **351**, 1058–1061 (2016).

[10] Gurzhi, R. N. Hydrodynamic effects in solids at low temperature. *Sov. Phys. Usp.* **11**, 255 (1968).

[11] Levitov, L. & Falkovich, G. Electron viscosity, current vortices and negative nonlocal resistance in graphene. *Nat. Phys.* **12**, 672–676 (2016).

[12] Aharon-Steinberg, A. *et al.* Direct observation of vortices in an electron fluid. *Nature* **607**, 74–80 (2022).

[13] Sulpizio, J. A. *et al.* Visualizing Poiseuille flow of hydrodynamic electrons. *Nature* **576**, 75–79 (2019).

[14] Ku, M. J. H. *et al.* Imaging viscous flow of the Dirac fluid in graphene. *Nature* **583**, 537–541 (2020).

[15] Krishna Kumar, R. *et al.* Superballistic flow of viscous electron fluid through graphene constrictions. *Nat. Phys.* **13**, 1182–1185 (2017).

[16] Gusev, G. M., Jaroshevich, A. S., Levin, A. D., Kvon, Z. D. & Bakarov, A. K. Stokes flow around an obstacle in viscous two-dimensional electron liquid. *Sci. Rep.* **10**:7860 (2020).

[17] Keser, A. C. *et al.* Geometric Control of Universal Hydrodynamic Flow in a Two-Dimensional Electron Fluid. *Phys. Rev. X* **11**, 031030 (2021).

[18] Damascelli, A., Hussain, Z. & Shen, Z. X. Angle-resolved photoemission studies of the cuprate superconductors. *Rev. Mod. Phys.* **75**, 473–541 (2003).

[19] Keimer, B., Kivelson, S. A., Norman, M. R., Uchida, S. & Zaanen, J. From quantum matter to high-temperature superconductivity in copper oxides. *Nature* **518**, 179–186 (2015).

[20] Chen, S. Di *et al.* Incoherent strange metal sharply bounded by a critical doping in Bi2212. *Science* **366**, 1099–1102 (2019).

[21] Hartnoll, S. A., Lucas, A. & Sachdev, S. Holographic quantum matter. *arXiv:1612.07324* (2016).

[22] Mackenzie, A. P. *et al.* Quantum oscillations in the layered perovskite superconductor $Sr_2RuO_4$. *Phys. Rev. Lett.* **76**, 3786 (1996).

[23] Mackenzie, A. P. *et al.* The Fermi Surface Topography of $Sr_2RuO_4$. *J. Phys. Soc. Japan* **67**, 385–388 (1998).

[24] Bergemann, C., Mackenzie, A. P., Julian, S. R., Forsythe, D. & Ohmichi, E. Quasi-two-dimensional Fermi liquid properties of the unconventional superconductor $Sr_2RuO_4$. *Adv. Phys.* **52**, 639–725 (2003).

[25] Wu, J. *et al.* Electronic nematicity in $Sr_2RuO_4$. *Proc. Natl. Acad. Sci.* **117**, 10654–10659 (2020).

[26] Mackenzie, A. P. & Maeno, Y. The superconductivity of $Sr_2RuO_4$ and the physics of spin-triplet pairing. *Rev. Mod. Phys.* **75**, 657 (2003).

[27] Kallin, C. Chiral p-wave order in $Sr_2RuO_4$. *Rep. Prog. Phys.* **75**, 042501 (2012).

[28] Mackenzie, A. P., Scaffidi, T., Hicks, C. W. & Maeno, Y. Even odder after twenty-three years: The superconducting order parameter puzzle of $Sr_2RuO_4$. *npj Quantum Mater.* **2**:40 (2017).

[29] Hussey, N., Mackenzie, A., Cooper, J., Maeno, Y. & Nishizaki, S. Normal-state magnetoresistance of $Sr_2RuO_4$. *Phys. Rev. B.* **57**, 5505 (1998).

[30] Bergemann, C., Julian, S. R., Mackenzie, A. P., Nishi Zaki, S. & Maeno, Y. Detailed topography of the fermi surface of $Sr2RuO_4$. *Phys. Rev. Lett.* **84**, 2662 (2000).

[31] Gardner, J. S., Balakrishnan, G. & Paul, D. M. Neutron powder diffraction studies of $Sr_2RuO_4$ and $SrRuO_3$. *Physica C* **252**, 303–307 (1995).

[32] Mackenzie, A. P. *et al.* Extremely Strong Dependence of Superconductivity on Disorder in $Sr_2RuO_4$. *Phys. Rev. Lett.* **80**, 161 (1998).

[33] Maeno, Y. *et al.* Two-Dimensional Fermi Liquid Behavior of the Superconductr $Sr_2RuO_4$. *J. Phys. Soc. Japan* **66**, 1405–1408 (1997).

[34] Maeno, Y., Nishizaki, S., Yoshida, K., Ikeda, S. & Fujita, T. Normal-State and Superconducting Properties of $Sr_2RuO_4$. *J. Low Temp. Phys.* **105**, 1577–1586 (1996).

[35] Paglione, J. *et al.* Elastic tensor of $Sr_2RuO_4$. *Phys. Rev. B* **65**, 220506(R) (2002).

[36] Barber, M. E., Gibbs, A. S., Maeno, Y., Mackenzie, A. P. & Hicks, C. W. Resistivity in the Vicinity of a van Hove Singularity: $Sr_2RuO_4$ under Uniaxial Pressure. *Phys. Rev. Lett.* **120**, 076602 (2018).

[37] Yasui, Y. *et al.* Spontaneous emergence of Josephson junctions in homogeneous rings of single-crystal $Sr_2RuO_4$. *npj Quantum Mater.* **5**:21 (2020).

[38] Squires, T. M. & Quake, S. R. Microfluidics: Fluid physics at the nanoliter scale. *Rev. Mod. Phys.* **77**, 977 (2005).

[39] Bandurin, D. A. *et al.* Fluidity onset in graphene. *Nat. Commun.* **9**:4533 (2018).

[40] Cooper, R. A. *et al.* Anomalous Criticality in the Electrical Resistivity of $La_{2-x}Sr_xCuO_4$. *Science* **323**, 603 (2009).

[41] Custers, J. *et al.* The break-up of heavy electrons at a quantum critical point. *Nature* **424**, 524–527 (2003).

[42] Grigera, S. A. Magnetic Field-Tuned Quantum Criticality in the Metallic Ruthenate $Sr_3Ru_2O_7$. *Science* **294**, 329–332 (2001).

[43] Hashimoto, K. *et al.* A sharp peak of the zero-temperature penetration depth at optimal composition in $BaFe_2(As_{1-x}P_x)_2$. *Science* **336**, 1554–1557 (2012).

[44] Hussey, N. E., Buhot, J. & Licciardello, S. A tale of two metals: Contrasting criticalities in the pnictides and hole-doped cuprates. *Rep. Prog. Phys.* **81**, 052501 (2018).

[45] Loram, J. W., Mirza, K. A., Cooper, J. R. & Liang, W. Y. Electronic specific Heat of $YBa_2Cu_3O_{6+x}$ from 1.8 to 300 K. *Phys. Rev. Lett.* **71**, 1740 (1993).

[46] Giraldo-Gallo, P. *et al*. Scale-invariant magnetoresistance in a cuprate superconductor. *Science* **361**, 479–481 (2018).

[47] Tesla, N. Valvular Conduit. *US Patent 1329559*. Feb. 1920